ACS OMEGA

Open Access



http://pubs.acs.org/journal/acsodf

Article

# Metallofullerenes as Robust Single-Atom Catalysts for Adsorption and Dissociation of Hydrogen Molecules: A Density Functional Study

Sehrish Sarfaraz, Muhammad Yar, Ajaz Hussain, Ahmed Lakhani, Adnan Gulzar, Muhammad Ans, Umer Rashid, Masroor Hussain, Shabbir Muhammad, Imene Bayach,* Nadeem S. Sheikh,* and Khurshid Ayub*

Cite This: *ACS Omega* 2023, 8, 36493−36505

Read Online

ACCESS | Metrics & More | Article Recommendations | Supporting Information

**ABSTRACT:** Hydrogen is currently considered as the best alternative for traditional fuels due to its sustainable and ecofriendly nature. Additionally, hydrogen dissociation is a critical step in almost all hydrogenation reactions, which is crucial in industrial chemical production. A cost-effective and efficient catalyst with favorable activity for this step is highly desirable. Herein, transition-metal-doped fullerene ($TM@C_{60}$) complexes are designed and investigated as single-atom catalysts for the hydrogen splitting process. Interaction energy analysis ($E_{int}$) is also carried out to demonstrate the stability of designed $TM@C_{60}$ metallofullerenes, which reveals that all the designed complexes have higher thermodynamic stability. Furthermore, among all the studied metallofullerenes, the best catalytic efficiency for hydrogen dissociation is seen for the $Sc@C_{60}$ catalyst $E_a$ = 0.13 eV followed by the $V@C_{60}$ catalyst $E_a$ = 0.19 eV. The hydrogen activation and dissociation processes over $TM@C_{60}$ metallofullerenes is further elaborated by analyzing charge transfer via the natural bond orbital and electron density difference analyses. Additionally, quantum theory of atoms in molecule analysis is carried out to investigate the nature of interatomic interactions between hydrogen molecules and $TMs@C_{60}$ metallofullerenes. Overall, results of the current study declare that the $Sc@C_{60}$ catalyst can act as a low cost, highly efficient, and noble metal-free single-atom catalyst to efficiently catalyze hydrogen dissociation reaction.

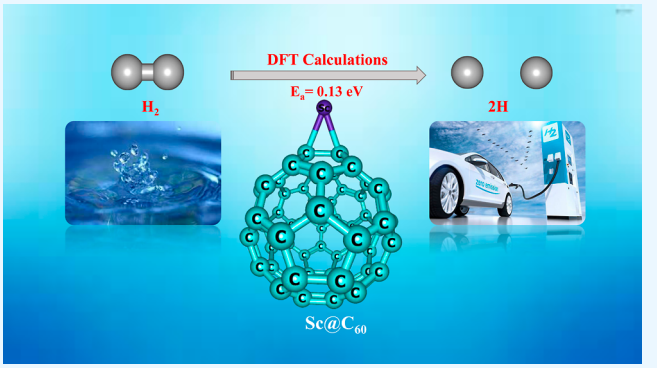


## 1. INTRODUCTION

In heterogeneous catalysis, the catalytic hydrogenation reaction is considered as one of the important reactions and is very vital for several industrial reactions, such as the hydrodechlorination[1,2] and hydrogenation of unsaturated hydrocarbons.[3−5] All these reactions involve hydrogen dissociation reaction (HDR) as a fundamental or elementary step. Moreover, upon dissociation, the hydrogen molecule dissociates into active atomic hydrogen, which is then adsorbed onto the catalyst surface or a support material, hence making it feasible to store a huge quantity of hydrogen at optimal pressures and temperatures.[6,7] Additionally, in the hydrogenation process, the hydrogen dissociation step is regarded as the rate-limiting or rate-determining steps. Therefore, for HDR on the metal catalysts, the understanding of the nature of active sites is the matter of intriguing interest for numerous studies.[8]

Furthermore, at the commercial level, catalytic adsorption and dissociation of hydrogen molecules has gained attention in the process of hydrogenation and dehydrogenation. In these reactions, hydrogen is the first to get adsorbed then dissociated; therefore, it is imperative to understand the fundamental steps involved in HDR and to design an electrocatalyst with high efficiencies.[9] Precious metal-supported catalysts have been broadly implemented for HDR due to their appropriate electronic structures, which allow $H_2$ molecules to get easily adsorbed on the metal catalyst and dissociate.[10] Moreover, the splitting ability of different metals vary depending on their associated intrinsic characteristics.[11] However, the scarcity and cost of numerous precious metal catalysts, such as palladium (Pd) and platinum (Pt), reduce their broad-scale utilization commercially.[12,13] To overcome this issue, various low-cost transition-metal (TM) catalysts are now extensively being

Received: July 27, 2023
Accepted: August 31, 2023
Published: September 18, 2023

explored with the key motif of designing practically viable catalysts with a high catalytic efficiency.

To accomplish this goal, two important aspects should be considered: finding an appropriate substrate or support to anchor the catalyst and to enhance the number of active sites on the electrocatalysts.[14−16] One of the most successful ways to improve the active site exposure and catalytic efficiency is the downsizing of the catalyst particles to a nano or even sub-nanocluster size.[17,18] Further decreasing the sub-nanoclusters to the atomic level well-defined catalysts, i.e., single-atom catalysts (SACs)[19] can afford to enhance the exposed active sites and provide maximal atom utilization, the ultimate goal of nanocatalysis.[20−22] Some of the chemical characteristics of single atoms in SACs are notably different from the nanoparticle or sub-nanometer clusters, the SACs have extraordinary selectivity, catalytic activity, and durability. Recently, the concept of SACs has been receiving a huge interest in heterogeneous catalysis. SAC improves the efficiency of atomic properties and possesses excellent catalytic performance.[23,24] Therefore, SAC, where chemical transformation is improved by dispersed metal atoms on the substrate material, has gained an ever-increasing interest because of unique reactivity and atom efficiency of SACs.[25−27] Minimal amounts of single atoms (SAs) are utilized by Ha et al. to enhance the active catalytic surface area and to improve the catalytic activity by coordinating the SAs in the defected sites of graphene (N-doped) and show high-performance 3d−5d TM SACs using the density functional theory (DFT).[28] One obstacle in this newly emerging field is the sintering of the dispersed metal atoms under extreme reaction conditions, which results in nanoparticle formation leading to an altered catalytic performance.[29] Second, these dispersed SAs are too mobile and generally suffer from significant aggregation, which drastically decrease the catalytic performance.[30] Another significant point to minimize or prevent agglomeration of single-metal atoms is finding an efficient and appropriate substrate to anchor the metal atom, which can provide support sites to robustly trap metal atoms.[31,32]

In this regard, carbon-based nanocages (fullerenes) have a high surface area with unique chemical and physical properties, making them outstanding zero-dimensional catalytic support materials. TM atom doping on the fullerene-based support (TM@fullerene) as SACs can improve the catalytic efficacy and lower the operational cost.[33] Among fullerenes, zero-dimensional buckminsterfullerene also known as the $C_{60}$ nanocage represents technologically suitable surfaces due to wide hollow interior of nanocage structure.[34] $C_{60}$ fullerene or buckminsterfullerene consists of 12 pentagons and 20 hexagons with a bond along each polygon to comply with the isolated pentagon rule (see Figure 1). Both exohedral and endohedral metal-doped $C_{60}$ fullerenes or metallofullerenes (TM@$C_{60}$) have gained extensive attention not only for scientific curiosity but also for practical implementations.[35−37] The metallofullerenes (TM@$C_{60}$) have been a subject of interest in many theoretical and experimental studies. Endohedral metallofullerenes (M@$C_{60}$, where M = Li, Ca, Ba, Sr, Sc, La, Ce, and La) have been immensely researched for applications in hydrogen storage.[38−40] Similarly, the stability, geometry, and electronic properties of $Sc_2$-doped (endohedral) $C_{66}$ metallofullerenes are investigated by Cui et al.[10] Therefore, the buckminsterfullerene ($C_{60}$ nanocage) can be effectively used as a support or substrate to anchor low-cost and abundant TM atoms for better catalytic performance.

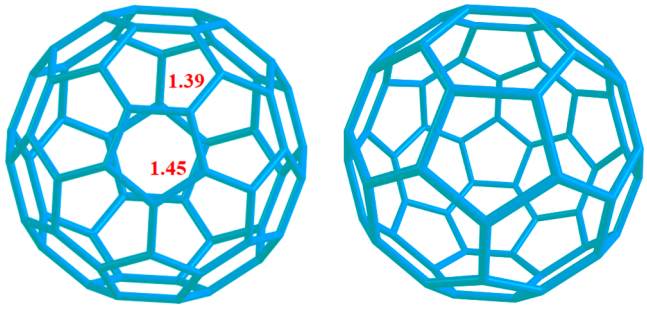


**Figure 1.** Optimized topology of $C_{60}$ fullerene (buckyball) with an icosahedral symmetry, where blue sticks present the C−C bonds in $C_{60}$ fullerene (a) with important bond lengths mentioned and (b) bare $C_{60}$.

Additionally, some theoretical studies are reported in the literature on the adsorption, stability, and catalytic activity systems like TM@$C_{60}$, which can further help to rationalize the above assumption. The interaction and adsorption of hydrogen molecule over exohedral metallofullerenes TM@$C_{60}$ (TM = V, Ti, and Cu) have been studied by Robledo et al.[41] Similarly, the stability and electronic properties of alkali metal-doped fullerene (AM@$C_{60}$, where AM = Li, Na, and K) have been investigated by Hamamoto et al. by using local density approximation based on the DFT.[42] Moreover, Ti- and Sc-supported boron carbide fullerenes ($B_{24}C_{24}$) have been theoretically explored as remarkable hydrogen storage materials by Ma et al.[43] Similarly, Hashemianzadeh and co-worker have shown alkali metal atom doping over $C_{60}$ fullerenes, which significantly enhanced the hydrogen adsorption capacity of doped fullerenes while following the set department of energy (DOE) standards.[44] Despite immense research reported on metallofullerenes, there is no systematic study reported yet on the TM-doped fullerenes (TM@$C_{60}$) as potential candidates for catalyzing for HDR.

Herein, we have chosen the most stable icosahedral symmetry of buckminsterfullerene ($C_{60}$ fullerene) as a substrate with the motivation of designing SAC for the hydrogen dissociation process.[23] First row TMs are supported on buckminsterfullerene (TM@$C_{60}$) to enhance the hydrogen adsorption and dissociation capacity. In the current study, first-row TM (Sc−Zn)-doped $C_{60}$ fullerenes are systemically studied for their stability, and catalytic performance for the dissociation process of hydrogen molecule. The investigation of the catalytic performance of TM@$C_{60}$ for the HDR is expected to displace precious noble metal catalysts for large-scale, sustainable, and commercial availability of hydrogen technology.

## 2. METHODOLOGY

All the DFT simulations are executed by using the Gaussian 09 package.[45] The calculations are performed at the B3LYP/6-31G(d,p) level of theory. B3LYP is a well-documented DFT functional commonly employed for the computation of thermodynamic stabilities, electronic characteristics, and mechanistic studies of fullerenes.[46−48] Furthermore, a B3LYP functional is a proven accurate and a reliable functional in the field of SAC.[49] Therefore, a B3LYP functional is chosen for geometry optimizations and energy profile analysis. The 6-31G(d,p) split valence Pople type basis set is used for all simulation with the added polarization function. Vibrational analysis is also performed to confirm the nature of the stationary points as minima or transition states (TSs) on the potential


https://doi.org/10.1021/acsomega.3c05477
ACS Omega 2023, 8, 36493−36505

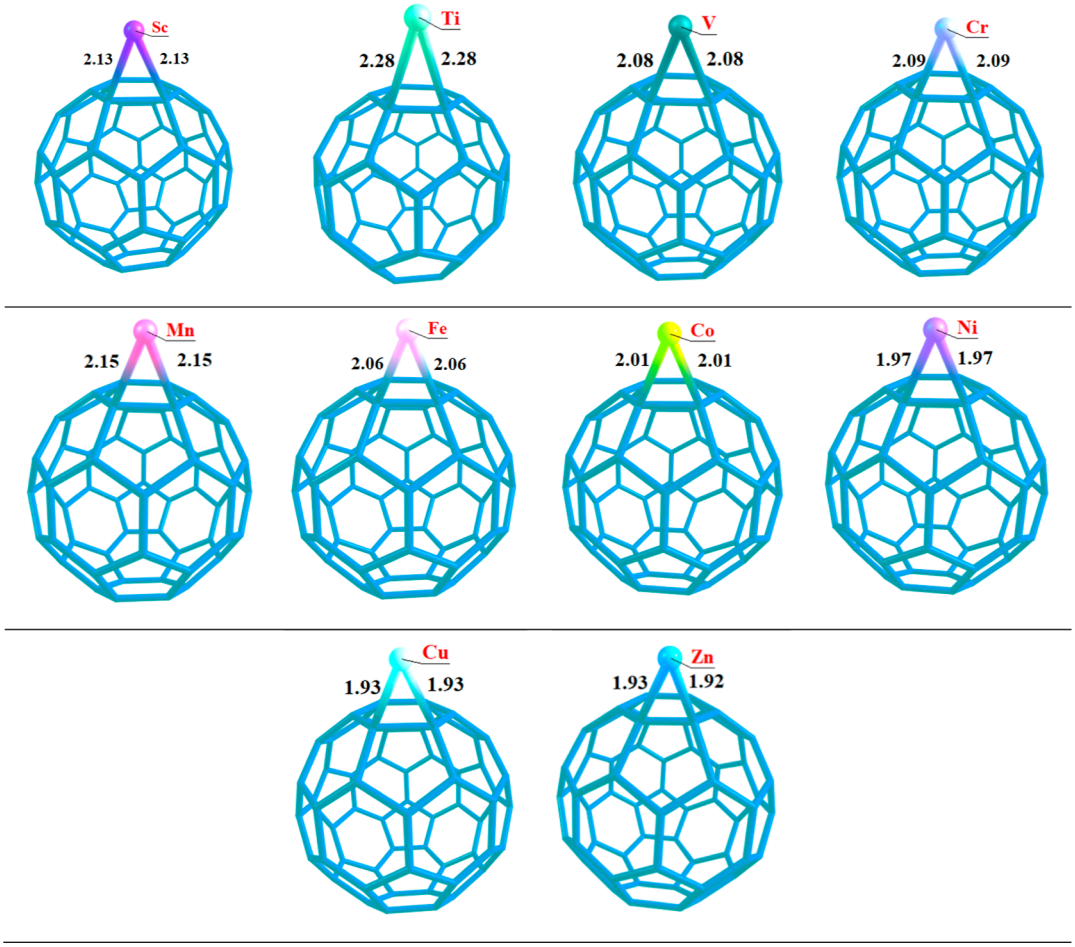


**Figure 2.** Optimized topologies of the most stable TMs@$C_{60}$ metallofullerenes at the B3LYP/6-31G(d,p) level of theory.

energy surface (PES) at the same level of theory. In the studied TM@$C_{60}$ complexes, the reactants and products are minima with no negative frequency is present, while TSs are corroborated from the presence of single negative frequencies. Moreover, the studied TSs are further confirmed from associated eigenvectors, which display the motion along the reaction coordinates.[50,51] The visualization of optimized geometries is done with the help of GaussView package and Chemcraft software.[52−54]

The TMs of first row are supported over the $C_{60}$ fullerene exohedrally and have been investigated to catalyze the hydrogen splitting reaction. To get the most stable TM@$C_{60}$ complex, TMs are doped at various positions; hexagon top, pentagon top, and C−C bridge. TMs show variable spin states; therefore, several lowest possible spin multiplicities, i.e., up to septet or octet are considered in the current study to get the thermodynamically most stable spin state. Further investigations of TM@$C_{60}$ complexes are performed over the most stable spin states.

Interaction energies ($E_{int}$) of TM-doped $C_{60}$ fullerenes are computed for the most stable spin states by using eq 1

$$\Delta E_{int} = E_{TM@C_{60}} - (E_{C60} + E_{TM}) \quad (1)$$

Here, $E_{TM@C_{60}}$, $E_{C_{60}}$, and $E_{TM}$ are the electronic energies of optimized geometries of TM@$C_{60}$ metallofullerenes, the bare $C_{60}$ surface and isolated TM atom in its stable spin state, respectively.

Moreover, Gibbss free energy of interaction is also evaluated to determine the entropic effects by the using the following equation

$$\Delta G = G_{TM@C_{60}} - (G_{C60} + G_{TM}) \quad (2)$$

Here, $G_{TM@C_{60}}$, $G_{C_{60}}$, and $G_{TM}$ are the Gibbs free energies of TM@$C_{60}$ metallofullerenes, bare $C_{60}$ surface, and isolated TM atom in its stable spin state, respectively.

To get insights into the binding strength of hydrogen molecules with designed TM@$C_{60}$ metallofullerenes, adsorption energy values are calculated by using eq 3. In eq 3, $E_{H_2TM@C_{60}}$ presents the total energy of hydrogen molecule adsorbed TM@$C_{60}$ metallofullerenes, whereas $E_{H_2}$ and $E_{TM@C_{60}}$ are the energies of isolated hydrogen molecule and optimized TM@$C_{60}$ metallofullerenes.

$$\Delta E_{ads}(H_2) = E_{H_2TM@C_{60}} - (E_{TM@C_{60}} + E_{H_2}) \quad (3)$$

The reaction energies ($\Delta E$) and activation barriers ($E_a$) are calculated using eqs 4 and 5, respectively. The HDR mechanism and pathways over variously designed TM@$C_{60}$ metallofullerenes are evaluated by comparing the energy barriers ($E_a$).[55]

$$\Delta E = E_P - E_R \quad (4)$$

$$E_a = E_{TS} - E_R \quad (5)$$

Here, $E_R$, $E_{TS}$, and $E_P$ present the energy of reactants (R), TS, and products (P), respectively. To further explore the



https://doi.org/10.1021/acsomega.3c05477
ACS Omega 2023, 8, 36493−36505

interaction of donor−acceptor species in the HDR mechanism over designed TM@$C_{60}$ metallofullerene, electron density differences (EDD) analysis is performed. Natural bond orbital (NBO) analysis is also performed at the level of theory, which helps to evaluate the nature of bonding interaction in terms of orbital interactions and charge transfer. Additionally, topological or quantum theory of atoms in molecule (QTAIM) analyses is carried out using the Multiwfn 3.8 program to evaluate the nature of interatomic interactions.[56]

## 3. RESULTS AND DISCUSSION

### 3.1. Geometry Optimization and Adsorption Energy.

The optimized geometry of buckyball ($C_{60}$ fullerene) is presented in Figure 1, which possesses the icosahedral symmetry with 20 hexagons (H) and 12 pentagons (P).[44] The titled fullerene $C_{60}$ nanocage exhibits two C−C symmetry unique bonds, associated with the junction between a five-membered ring (pentagon) and a six-membered ring (hexagon) and at the junction of two six-membered rings (two hexagons), as shown in Figure 1a,b. The fully relaxed geometry of $C_{60}$ fullerene reveal the C−C bond lengths of 1.45 and 1.39 Å for the above discussed two unique bond lengths (see Figure 1a). The computed bond lengths for $C_{60}$ fullerene are nicely corroborated with the previously reported DFT data as well as X-ray diffraction data.[57,58] During the optimization process, initially the TM atom is over the top of hexagon and pentagon rings as well as placed above the C−C bridge. The results reveal that the exohedral doping over the bridge site (junction) is the most stable site for doping in all TM@$C_{60}$ complexes. All the geometry optimization simulations are carried out without symmetry constraints. Moreover, the stationary points of optimized geometries have also been corroborated via vibrational frequency calculations.

Moreover, for all the considered TM atoms, four of the lowest possible spin states of each metallofullerene (TM@$C_{60}$) are investigated to get the most stable spin state. Doublet is observed as the most stable spin state for Sc@$C_{60}$ and Cu@$C_{60}$ and quartet for V@$C_{60}$ and Co@$C_{60}$. Similarly, sextet is observed as the most stable spin state for the Mn@$C_{60}$ complex. In the case of Ti@$C_{60}$, Cr@$C_{60}$, and Fe@$C_{60}$, quintet is the most stable state, whereas Ni@$C_{60}$ and Zn@$C_{60}$ complexes are triplet and singlet stable spin states, respectively. The relative energies (au) of considered spin states of TM-doped $C_{60}$ fullerenes are summarized in Table S1 (Supporting Information), whereas the optimized topologies of the most stable spin states and their associated interaction energies are presented in Figure 2 and Table 1, respectively.

Bond interaction distances and interaction energies are two crucial parameters to evaluate the thermodynamic stability of any system.[59] In Figure 2, the interaction bond distances between the considered TMs and $C_{60}$ fullerene are calculated in the range of 1.92 to 2.28 Å. In all studied metallofullerenes, the least TM−C interaction distance is observed for the Zn@$C_{60}$ complex (1.92 and 1.93 Å), followed by the Cu@$C_{60}$ complex (1.93 Å) for the Cu−C bond. The lower value of interaction distance in the case of Cu@$C_{60}$ metallofullerene is also corroborated nicely with the highest interaction energy ($\Delta E_{int}$) value for this complex (−2.13 eV). Whereas the highest TM−C interaction distance of 2.28 Å is obtained for the Ti@$C_{60}$ complex for each Ti−C bond among all the considered metallofullerenes. Moreover, in the case of early TM-doped $C_{60}$ metallofullerenes, an irregular trend is observed for the TM−C bond length from Sc to Mn. However, for late transition meta-doped complexes, a gradual decrease in interaction distances is seen as the atomic number increases from Fe to Zn. In late transition-meta-doped metallofullerenes, the interaction distance gradually decreases with the decrease in the number of unpaired electrons. The computed interaction distances between TM atoms and $C_{60}$ fullerene for all the studied metallofullerenes are almost comparable with their corresponding TM−C reported bond lengths.[55]

**Table 1. Summary of Interaction Energies for TMs@$C_{60}$ Metallofullerenes ($\Delta E_{int}$), Gibbs Free Energy ($\Delta G$), Adsorption Energies for $H_2$ Adsorbed TM@$C_{60}$ ($\Delta E_{ads}$), and Calculated Energy Barriers for the Hydrogen Splitting Process ($\Delta E_a$)[a]**

| complexes | $\Delta E_{int}$ ($\Delta G$) | complexes | $\Delta E_{ads}$ (eV) | $\Delta E_a$ (eV) |
|---|---|---|---|---|
| Sc@$C_{60}$ | −1.19 (−0.39) | $H_2$Sc@$C_{60}$ | −0.67 | 0.13 |
| Ti@$C_{60}$ | −1.83 (−1.57) | $H_2$Ti@$C_{60}$ | −0.13 | 0.74 |
| V@$C_{60}$ | −1.14 (−0.33) | $H_2$V@$C_{60}$ | −0.75 | 0.19 |
| Cr@$C_{60}$ | −1.03 (−0.82) | $H_2$Cr@$C_{60}$ | −0.88 | 0.54 |
| Mn@$C_{60}$ | −0.68 (−0.45) | $H_2$Mn@$C_{60}$ | −0.26 | 0.23 |
| Fe@$C_{60}$ | −0.42 (−0.11) | $H_2$Fe@$C_{60}$ | −0.41 | 0.43 |
| Co@$C_{60}$ | −0.95 (−0.64) | $H_2$Co@$C_{60}$ | −0.48 | 0.42 |
| Ni@$C_{60}$ | −0.98 (−0.66) | $H_2$Ni@$C_{60}$ | −0.77 | 0.93 |
| Cu@$C_{60}$ | −2.13 (−1.80) | $H_2$Cu@$C_{60}$ | −0.71 | 0.74 |
| Zn@$C_{60}$ | −0.15 (0.19) | $H_2$Zn@$C_{60}$ | −0.01 | 0.50 |

[a]All values are in eV.

Beside interaction distances, interaction energies of TM@$C_{60}$ metallofullerenes are also computed by using eq 1, and the values are presented in Table 1. In all studied metallofullerenes, the negative value of interaction energies reveals that the doping of TM atoms over the $C_{60}$ fullerene is thermodynamically a feasible process. Among the studied metallofullerenes, the highest interaction energy is seen for the Cu@$C_{60}$ complex (−2.13 eV) followed by Ti@$C_{60}$ (−1.83 eV) and Sc@$C_{60}$ (−1.19 eV), which reveals the thermodynamic stability of these metallofullerenes. The highest value of $E_{int}$ for the Cu@$C_{60}$ complex is strongly correlated with the lower TM−C bond length (see Figure 2 for details). Additionally, Gibbs free energy of interaction is also computed to consider the entropic effects by using eq 2. The values of Gibbs free energy of interaction are reported in parentheses along with electronic interaction energies for the studied TM@$C_{60}$ metallofullerenes (see Table 1). Overall, the same trend is observed in the case of Gibbs free energy of adsorption as in the electronic interaction energies. Among the studied metallofullerenes, the highest Gibbs free energy is seen for the Cu@$C_{60}$ complex (−1.80 eV) followed by Ti@$C_{60}$ (−1.57 eV), which reveals a similar trend of the thermodynamic stability of these metallofullerenes as seen for electronic interaction energies.

Overall, the calculated interaction energy values are observed in the range of −0.15 to −2.13 eV for all the considered metallofullerenes. The lowest interaction energy and positive Gibbs free energy observed for the Zn@$C_{60}$ complex is strongly correlated with the previously reported literature.[60] Furthermore, no structural deformation is noticed upon geometry optimization in any metallofullerene.

### 3.2. Adsorption of Hydrogen Molecule over TM@$C_{60}$ Catalysts.

Initially, the $H_2$ molecule is placed at the side edge position of TMs and carbon atoms of $C_{60}$ fullerene as well as over the top of TM and in all the considered metallofullerenes, the side edge position is more favorable energetically for hydrogen adsorption. Therefore, adsorption energy ($E_{ads}$) values


https://doi.org/10.1021/acsomega.3c05477
ACS Omega 2023, 8, 36493−36505

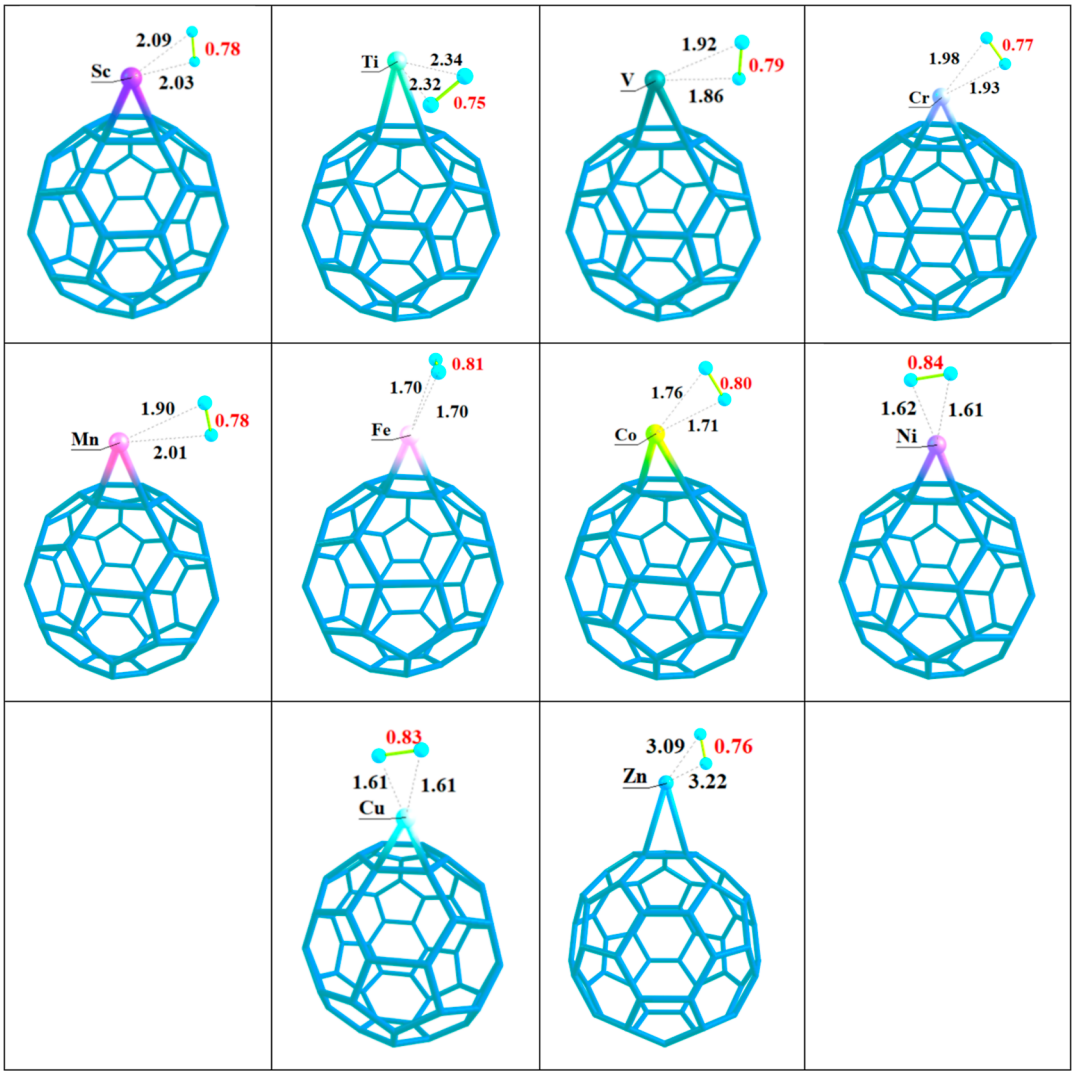


**Figure 3.** Optimized structures of hydrogen adsorbed TM@$C_{60}$ metallofullerenes at the B3LYP/6-31G(d,p) level of theory.

are calculated for the adsorption of $H_2$ molecule at the side edge position in all the studied metallofullerenes (see Figure 3 and Table 1). In general, the more negative the value of adsorption energy is, the more rigidly and strongly the hydrogen molecule interacts on the surface of catalyst, which results in the favorable adsorption process. On the other hand, the positive value of adsorption energy corresponds to an endothermic and a thermodynamically unfavorable adsorption process. Therefore, the higher adsorption energy value of hydrogen-adsorbed TM@$C_{60}$ metallofullerenes reveal higher thermodynamic stability. The calculated hydrogen adsorption energy values are observed in the range of −0.01 to −0.88 eV, which reveal that the process of hydrogen molecule adsorption is an energetically favorable process without any structural distortion in all the studied metallofullerenes. The highest hydrogen adsorption energy is obtained for the Cr@$C_{60}$ complex (−0.88 eV), followed by Ni@$C_{60}$ (−0.77 eV), Cu@$C_{60}$ (−0.71 eV), and Sc@$C_{60}$ (−0.67 eV) catalysts (Table 1). During the adsorption process, the hydrogen molecule approaches from the side edge location in all the designed metallofullerene complexes.

Similarly, upon hydrogen molecule adsorption over TM@$C_{60}$ metallofullerenes, the H−H bond length is calculated in the range of 0.75 to 0.84 Å, as given in Figure 3. In all the designed complexes, the H−H bond distance is slightly elongated as compared to the bond length of isolated hydrogen molecules (0.74 Å), which is primarily attributed to stronger TM−H and C−H bond interactions, which ultimately results in debilitating the H−H bond. It is further observed that TM−H interaction distances are seen in the wider range vary from 1.61 to 3.22 Å (see Figure 3).

In summary, the highest value of hydrogen adsorption energy is seen for the Cr@$C_{60}$ complex, whereas the lowest adsorption energy value among all the considered metallofullerenes is obtained for the Zn@$C_{60}$ catalyst (−0.01 eV). Overall, the process of hydrogen molecule adsorption over TM@$C_{60}$ metallofullerenes results in a slight increase of H−H bond distance, which further reveals the activation of $H_2$ molecule on the designed catalysts.

**3.3. Dissociation of Hydrogen Molecule over TM@$C_{60}$ Metallofullerenes.** The HDR is one of the most prominent reactions on the catalytic surfaces. This reaction involves the breaking of a molecular covalent bond, with simultaneous formation of new atomic bonds; hence, an efficient catalyst is required to catalyze this reaction. To explore catalytic activity of the designed TM@$C_{60}$ catalysts for the cleavage of $H_2$ molecules, the HDR is studied through the heterolytic pathway. The energetics of reaction pathway for the HDR over designed TM@$C_{60}$ metallofullerenes are graphically presented in Figure


https://doi.org/10.1021/acsomega.3c05477
ACS Omega 2023, 8, 36493−36505

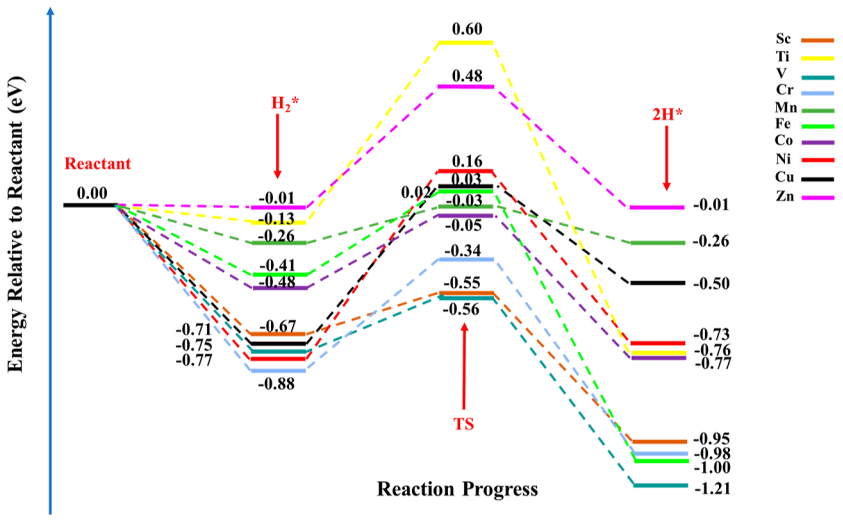


**Figure 4.** HDR energy profiles for TM@$C_{60}$ metallofullerenes (TM = Sc−Zn) and intermediate ($H_2$*) state, TS, and final state (2H*) energies are relative to reactant and expressed in eV.

4. The energy diagram in Figure 4 declares that both reactant ($H_2$*) and product (2H*) adsorption is thermodynamically favorable in all the designed TM@$C_{60}$ catalysts, which corroborates from the calculated negative energies of these states. The catalytic HDR has three basic steps: step I involves the adsorption of $H_2$ over the catalyst surface resulting in an $H_2$* state (intermediate state), step II, the splitting of H−H bond of hydrogen molecule, and step II, the dissociated atomic hydrogens (2H*) bind on the corresponding active binding sites.

The energy barriers reported in Table 1 reveal that the lowest hydrogen dissociation energy barrier is obtained for the Sc@$C_{60}$ catalyst (0.13 eV), while the maximum barrier is seen for the Ni@$C_{60}$ catalyst (0.93 eV). Furthermore, the energy barrier for $H_2$ dissociation over V@$C_{60}$ catalysts is 0.19 eV, which is quite low as compared to the rest of the studied catalysts. After Sc@$C_{60}$ and V@$C_{60}$ catalysts, the third lowest energy barrier is computed for the Mn@$C_{60}$ catalyst (0.23 eV) followed by Co@$C_{60}$, Fe@$C_{60}$, Zn@$C_{60}$, and Cr@$C_{60}$ with energy barriers of 0.42, 0.43, 0.50, and 0.54 eV, respectively. For the remaining designed metallofullerenes, the energy barriers for the HDR are 0.74 eV (Cu@$C_{60}$), 0.74 eV (Ti@$C_{60}$), and 0.93 eV (Ni@$C_{60}$). The H−H bond distances of hydrogen molecule show more pronounced elongation at the TS and lie in a range of 0.97−1.16 Å for the studied catalysts. Elongation in H−H bond distances reveals that the $H_2$ molecule is fully activated over designed metallofullerene catalysts and promote a facile hydrogen splitting process (Figure 5).

Herein, the metallofullerene catalysts with the best performance for HDR are taken as representative models for the detailed discussion, i.e., Sc@$C_{60}$, V@$C_{60}$, and Mn@$C_{60}$ catalysts. Moreover, the detailed reaction pathway of these representative TM@$C_{60}$ metallofullerene catalysts with a better efficiency (Sc@$C_{60}$, V@$C_{60}$, and Mn@$C_{60}$), is given in Figure 5a−c. Additionally, the detailed dissociation reaction pathway energy diagrams of the remaining designed metallofullerenes are presented in the Supporting Information (Figure S1a−g). It is obvious from Figure 5a that, on the Sc@$C_{60}$ catalyst surface, initially the $H_2$ molecule gets adsorbed from the side edge site where hydrogen atoms are approaching toward the Sc atom for the hydrogen splitting process ($H_2$* → 2H*). The adsorption of hydrogen molecules is followed by dissociation, which results in the formation of atomic hydrogen, which diffuse to the TM site and C site positions each. This $H_2$ splitting step requires overcoming an energy barrier of 0.13 eV (2.99 kcal/mol). In the dissociation process, the H−H bond length is a key parameter, which illustrates the stability of TS. In the case of Sc@$C_{60}$ catalyst, at TS the H−H bond distance extends to 1.05 Å, which is about 0.78 Å at the intermediate state. This much pronounced elongation in the H−H bond distance at TS declares that the hydrogen molecule is fully activated over Sc@$C_{60}$ metallofullerene. TS further declares that the hydrogen dissociation splitting process passed through heterolytic cleavage of H−H bond. At TS, the hydrogen molecule is dissociated into atomic hydrogen, which on the product (2H*) side migrated to the Sc active site and C site (see Figure 5a for details), along with a release of −0.40 eV of energy. Moreover, the C−H and Sc−H bond lengths are further reduced upon binding to 1.14 and 1.51 Å from 1.53 and 1.88 Å, respectively. The enthalpy of $H_2$Sc@$C_{60}$ complex (product) is −0.95 eV and, hence, declare stability of product (dissociated hydrogen) as compared to molecular hydrogen (−0.67 eV).

Similarly, the V@$C_{60}$ catalyst displays the second least hydrogen dissociation barrier and the detailed energy profile along with the optimized geometries are presented in Figure 5b. In this case, the computed H−V bond lengths are 1.92 and 1.86 Å at the intermediate state ($H_2$*). Similarly, the H−H bond length at the intermediate state is about 0.79 Å, which elongates to 1.06 Å at the TS (Figure 5b). The calculated activation barrier for the splitting of hydrogen molecule over the V@$C_{60}$ catalyst is about 0.19 eV (4.38 kcal/mol). The Ti−H and C−H interaction bond distances are reduced at the TS to 1.74 and 1.52 Å, respectively, which shows the strong interaction of hydrogen molecule with the catalyst surface. When the hydrogen molecule is dissociated into atoms, the atomic hydrogen binds at the V site (V−H) and carbon site (C−H) with 1.72 and 1.10 Å bond distances, respectively.

In the case of Mn@$C_{60}$ metallofullerene catalyst, the H−H bond length of initially adsorbed $H_2$ molecule is 0.78 Å, which enlarges to 1.02 Å at the TS. Just like Sc@$C_{60}$ and V@$C_{60}$ catalysts, the hydrogen dissociation process over the Mn@$C_{60}$ catalyst also occurs on the side edge location via heterolytic cleavage. Upon dissociation atomic hydrogen gets adsorbed at the metal site and carbon site positions. In this case, the


https://doi.org/10.1021/acsomega.3c05477
ACS Omega 2023, 8, 36493−36505

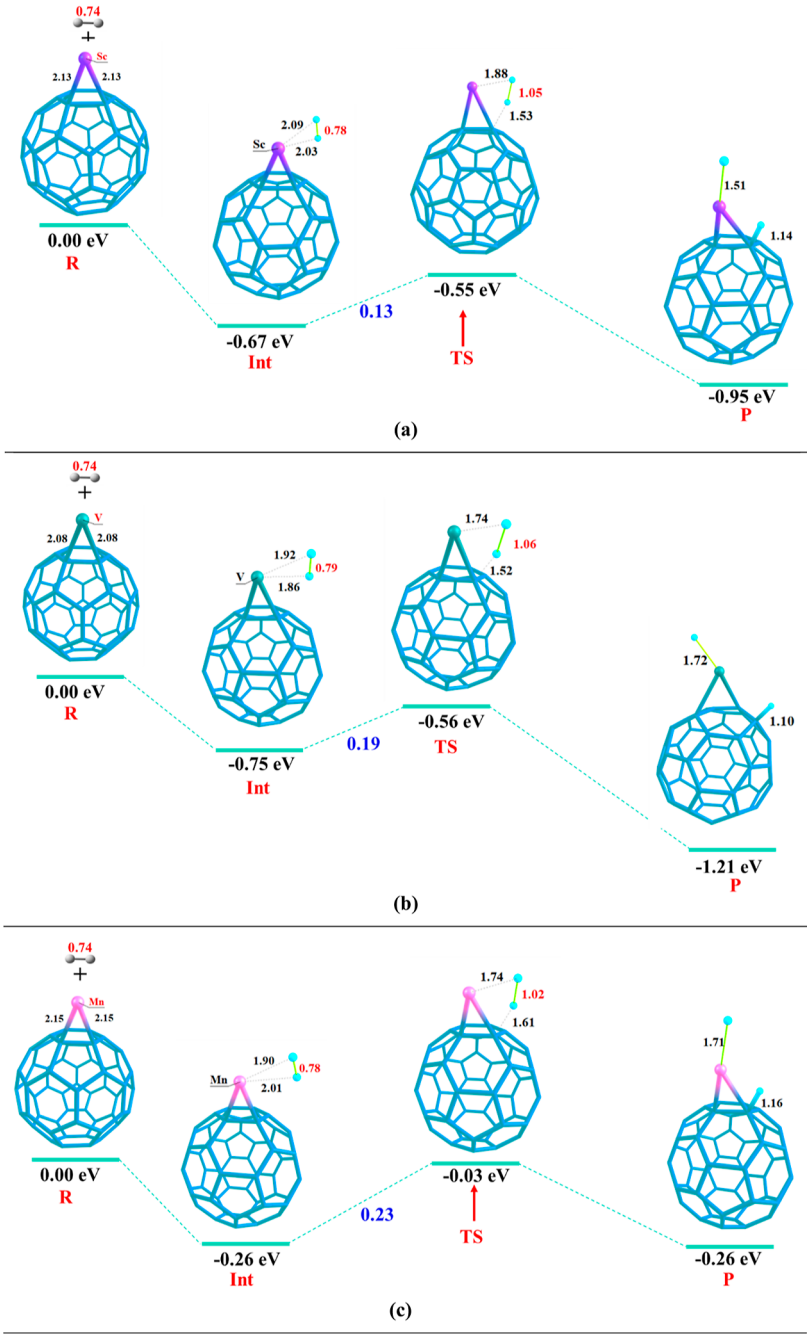


**Figure 5.** Schematic representation of reactants, intermediate state (Int), TS, and final state (products) are illustrated with important bond lengths mentioned (H, cyan blue; Sc, purple; Ti, green; Mn, pink; C−C bond, blue sticks). (a) Sc@$C_{60}$, (b) V@$C_{60}$, and (c) Mn@$C_{60}$.

hydrogen dissociation step needs to overcome an energy dissociation barrier of 0.23 eV (5.30 kcal/mol). The Sc−H and C−H bond distances at the TS are reduced to 1.74 and 1.61 Å from their corresponding interaction distances at the intermediate state, respectively (see Figure 5c). Then, the dissociated hydrogen independently binds over carbon sites and metal adsorption sites with bond lengths of 1.16 Å (C−H) and 1.71 Å (Mn−H). Moreover, the enthalpy of final state (2H* + Mn@$C_{60}$) is −0.26 eV, which is equivalent to the enthalpy of intermediate state ($H_2$* + Mn@$C_{60}$), which reveals the thermodynamic stability of both reactant and product states. The observed H−H bond distances are more pronounced or elongated than the previously reported literature over different TM-doped catalysts.[61−64]

Overall, the hydrogen dissociation energy barriers over various designed TM@$C_{60}$ metallofullerenes are observed in the broad range of 0.13−0.93 eV. Among all the studied TM@$C_{60}$ metallofullerenes, the lowest activation barrier is seen for the Sc@$C_{60}$ complex (0.13 eV), which can be attained very easily under mild conditions, which is a fundamental criterion for hydrogenation reactions. The computed energetics declare that Sc@$C_{60}$ metallofullerenes have a remarkable catalytic performance for the HDR followed by the V@$C_{60}$ catalyst. The best catalytic activity of Sc@$C_{60}$ catalyst is attributed to the highest NBO charge transfer from the scandium (Sc) metal atom as compared to the rest of the designed transition metallofullerenes. Corma et al. calculated the $H_2$ dissociation activity of $Au_{25}$ cluster at various active sites and found a broad range of


https://doi.org/10.1021/acsomega.3c05477
ACS Omega 2023, 8, 36493−36505

energy barriers 2.14−20.58 kcal/mol for the HDR.[65] Similarly, the energy barrier for hydrogen dissociation over the Sc@$C_{60}$ complex (0.13 eV) is much lower than the noble metal-doped catalyst (Au/$TiO_2$), where the energy barrier for hydrogen dissociation is 0.54 eV.[66] Sc@$C_{60}$ can act as a remarkable SAC, which gives the best catalytic performance for the HDR.

**3.4. Natural Bond Orbital and Electron Density Difference Analyses.** NBO and EDD analyses are also performed to elaborate the process of hydrogen molecule activation and dissociation over the designed metallofullerenes. NBO analysis is performed to evaluate the exact amount of transfer of charge from TMs (3d orbitals) upon hydrogen adsorption (see Table 2). The calculated values of NBO charges on TMs, hydrogen atoms, and corresponding carbon atom of hydrogen-adsorbed TM@$C_{60}$ complexes are listed in Table 3. In all the designed $H_2$* + TM@$C_{60}$ metallofullerenes, the TMs bear positive NBO charges, while the hydrogen atom (H1) directly interacting with the metal atom has a negative NBO charge value. Similarly, the negative NBO charge is observed over the C center interacting directly with the hydrogen atom H(2), which possesses the positive NBO charge. NBO analysis corroborates the electropositive nature of TM atoms as the charge is being transferred from TMs to $C_{60}$ fullerene and H atom. In all the designed metallofullerenes, the trend of NBO charge transfer is consistent, i.e., from TMs to H atom and $C_{60}$ fullerene. However, the carbon atom interacting with H(2) atoms is extracting charge from the same hydrogen atom, thus revealing the heterolytic cleavage of hydrogen molecule. The highest value of NBO charge transfer is seen for the Sc metal (+1.026 e), whereas the minimum NBO charge transfer is obtained for the Cu metal (+0.641 e). It is observed that the amount of charge transfer decreases gradually with the increase in the atomic number from Sc to Zn, which is nicely correlated with the already reported literature.

**Table 2. Summary of NBO Charge-Transfer Results of Designed Hydrogen Adsorbed TM@$C_{60}$ Metallofullerenes**

| complexes | H(1) (e) | TM (e) | H(2) (e) | C (e) |
|---|---|---|---|---|
| $H_2$Sc@$C_{60}$ | −0.224 | 1.026 | 0.100 | −0.345 |
| $H_2$Ti@$C_{60}$ | −0.227 | 0.944 | 0.141 | −0.303 |
| $H_2$V@$C_{60}$ | −0.204 | 0.929 | 0.120 | −0.308 |
| $H_2$Cr@$C_{60}$ | −0.261 | 0.963 | 0.113 | −0.290 |
| $H_2$Mn@$C_{60}$ | −0.197 | 0.920 | 0.111 | −0.298 |
| $H_2$Fe@$C_{60}$ | −0.191 | 0.882 | 0.119 | −0.279 |
| $H_2$Co@$C_{60}$ | −0.183 | 0.773 | 0.113 | −0.270 |
| $H_2$Ni@$C_{60}$ | −0.186 | 0.763 | 0.113 | −0.260 |
| $H_2$Cu@$C_{60}$ | −0.284 | 0.641 | 0.116 | −0.215 |
| $H_2$Zn@$C_{60}$ | −0.176 | 0.662 | 0.136 | −0.204 |

In this case, the best performing catalyst is Sc@$C_{60}$ metallofullerenes for which a NBO charge of +1.026 e is calculated on the Sc metal atom, which is the highest charge transfer among all the designed metallofullerenes. Similarly, a NBO charge of −0.224 e is observed over the hydrogen atom H(1) interacting with the Sc metal atom. At TSs, a charge of −0.345 e is seen for the representative C atom interacting with H(2) atoms, while adsorbed hydrogen atom H(2) exhibits a NBO charge of +0.100 e. The positive NBO charge on the TM center (Sc) indicates the electropositive behavior of TM atoms. Similarly, the positive value of NBO charge on H(2) atoms declares the transfer of charge from the adsorbed hydrogen atom to the representative C atom participating in the TS. In summary, the NBO analysis reveals that strong binding interactions exist between the TM atom and adsorbed hydrogen molecule, which causes the activation and dissociation of adsorbed molecule. The NBO charge transfer on interacting sites is significantly responsible for the elongation of H−H bond, thus facilitating the dissociation of hydrogen over TM@$C_{60}$ metallofullerenes. Moreover, charge-transfer analysis unveils the transfer of NBO charge from TMs to the adsorbed molecule, which results in filling up $\sigma^*$ of hydrogen molecule, consequently, promotes the HDR.

To further elaborate the NBO results through visualization, EDD analysis is performed for all $H_2$* + TM@$C_{60}$ metallofullerenes. The plotted EDD isosurfaces for designed $H_2$* + TM@$C_{60}$ metallofullerenes are presented in Figure 6. The

**Table 3. Summary Topological Parameters Obtained for Hydrogen Adsorbed TM@$C_{60}$ Metallofullerenes via QTAIM Analyses**

| complexes | analyte−$H_2$ | $\rho$ (a.u) | $\nabla^2\rho$ (a.u) | $G_{(r)}$ (a.u) | $V_{(r)}$ (a.u) | $H_{(r)}$ (a.u) | $-V/G$ |
|---|---|---|---|---|---|---|---|
| $H_2$Sc@$C_{60}$ | Sc−H(1) | 0.064 | 0.155 | 0.049 | −0.059 | −0.010 | 1.20 |
| | C−H(2) | 0.093 | −0.076 | 0.031 | −0.081 | −0.050 | 2.61 |
| $H_2$Ti@$C_{60}$ | Ti−H(1) | 0.123 | −0.118 | 0.033 | −0.096 | −0.062 | 2.91 |
| | C−H(2) | 0.068 | 0.158 | 0.052 | −0.065 | −0.013 | 1.25 |
| $H_2$V@$C_{60}$ | V−H(1) | 0.080 | 0.232 | 0.074 | −0.090 | −0.016 | 1.22 |
| | C−H(2) | 0.111 | −0.072 | 0.033 | −0.083 | −0.051 | 2.52 |
| $H_2$Cr@$C_{60}$ | Cr−H(1) | 0.090 | 0.236 | 0.084 | −0.109 | −0.025 | 1.30 |
| | C−H(2) | 0.106 | −0.081 | 0.028 | −0.075 | −0.048 | 2.68 |
| $H_2$Mn@$C_{60}$ | Mn−H(1) | 0.079 | 0.187 | 0.070 | −0.094 | −0.024 | 1.34 |
| | C−H(2) | 0.092 | −0.029 | 0.028 | −0.063 | −0.035 | 2.25 |
| $H_2$Fe@$C_{60}$ | Fe−H(1) | 0.081 | −0.093 | 0.081 | −0.105 | −0.054 | 1.45 |
| | C−H(2) | 0.089 | −0.019 | 0.028 | −0.062 | −0.033 | 1.96 |
| $H_2$Co@$C_{60}$ | Co−H(1) | 0.101 | 0.178 | 0.091 | −0.138 | −0.046 | 1.52 |
| | C−H(2) | 0.100 | −0.040 | 0.031 | −0.071 | −0.041 | 2.29 |
| $H_2$Ni@$C_{60}$ | Ni−H(1) | 0.111 | 0.173 | 0.105 | −0.166 | −0.061 | 1.58 |
| | C−H(2) | 0.098 | −0.025 | 0.032 | −0.070 | −0.038 | 2.19 |
| $H_2$Cu@$C_{60}$ | Cu−H(1) | 0.130 | 0.034 | 0.095 | −0.181 | −0.086 | 1.91 |
| | C−H(2) | 0.078 | 0.055 | 0.034 | −0.055 | −0.020 | 1.62 |
| $H_2$Zn@$C_{60}$ | Zn−H(1) | 0.067 | 0.101 | 0.051 | −0.077 | −0.026 | 1.51 |
| | C−H(2) | 0.115 | −0.087 | 0.035 | −0.091 | −0.057 | 2.60 |



https://doi.org/10.1021/acsomega.3c05477
ACS Omega 2023, 8, 36493−36505

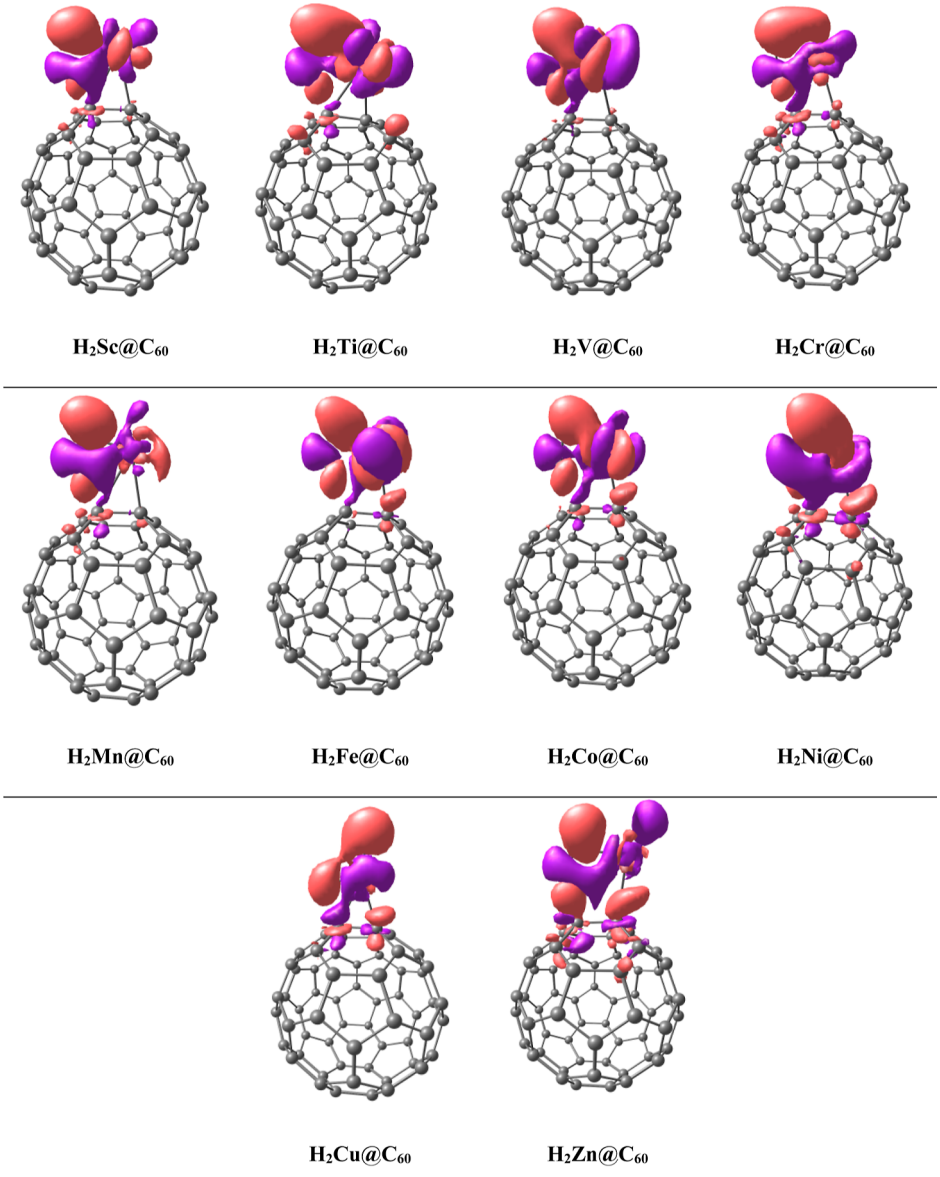


**Figure 6.** EDD isosurfaces of designed hydrogen-adsorbed TMs@$C_{60}$ metallofullerenes, pink isosurfaces present the electronic density accumulation, while purple isosurfaces show the electronic density depletion.

isosurfaces of EDD analysis exhibit pink and purple patches, which show the transfer of charge upon hydrogen adsorption over the studied metallofullerenes. Isosurfaces in purple color reveal the region with electron density depletion, whereas pink-colored isosurfaces show the region with electron density accumulation. It is obvious from Figure 6 that the charge is being transferred from TMs to H(1) and from H(2) to representative C atom upon hydrogen adsorption in all considered $H_2$* + TM@$C_{60}$ metallofullerenes. In all metallofullerene complexes, the purple isosurfaces appear mainly over the TM atom and H(2) atom revealing the depletion of electronic density. Similarly, pink colored patches appear over H(1) atoms and C atoms of $C_{60}$ fullerene. The above-discussed outcomes of EDD analysis are consistent with the charge-transfer analysis results. Moreover, it is further validated that the process of charge-transfer promotes the process of filling up of antibonding orbital of hydrogen molecule, hence making the HDR more feasible over TM@$C_{60}$ metallofullerenes.

**3.5. QTAIM Analyses.** Bader's QTAIM analyses are carried out to investigate the nature of interatomic interactions between the hydrogen molecule and TMs@$C_{60}$ metallofullerenes. The topological parameters obtained through QTAIM analyses are helpful in demonstrating the nature of interatomic interactions along BCPs (bond critical points). The important topological parameters are electron density ($\rho$), Laplacian of electronic density ($\nabla^2\rho$), kinetic energy density ($G_{(r)}$), potential energy ($V_{(r)}$), and total energy density ($H_{(r)}$). Electron density helps to evaluate the strength of a bond at BCP, whereas Laplacian of electronic density helps to examine the nature of interaction. Additionally, the $-V/G$ ratio also helps to evaluate the inter-atomic interactions, i.e., $-V_{(r)}/G_{(r)} > 2$ corresponds to covalent bonding, whereas $-V_{(r)}/G_{(r)} < 1$ shows weak interactions. The extracted values of topological parameters obtained through QTAIM analyses are summarized in Table 3, whereas the QTAIM molecular plots of the designed $H_2$-adsorbed TM@$C_{60}$ metallofullerenes are given in Figure 7.



https://doi.org/10.1021/acsomega.3c05477
ACS Omega 2023, 8, 36493−36505

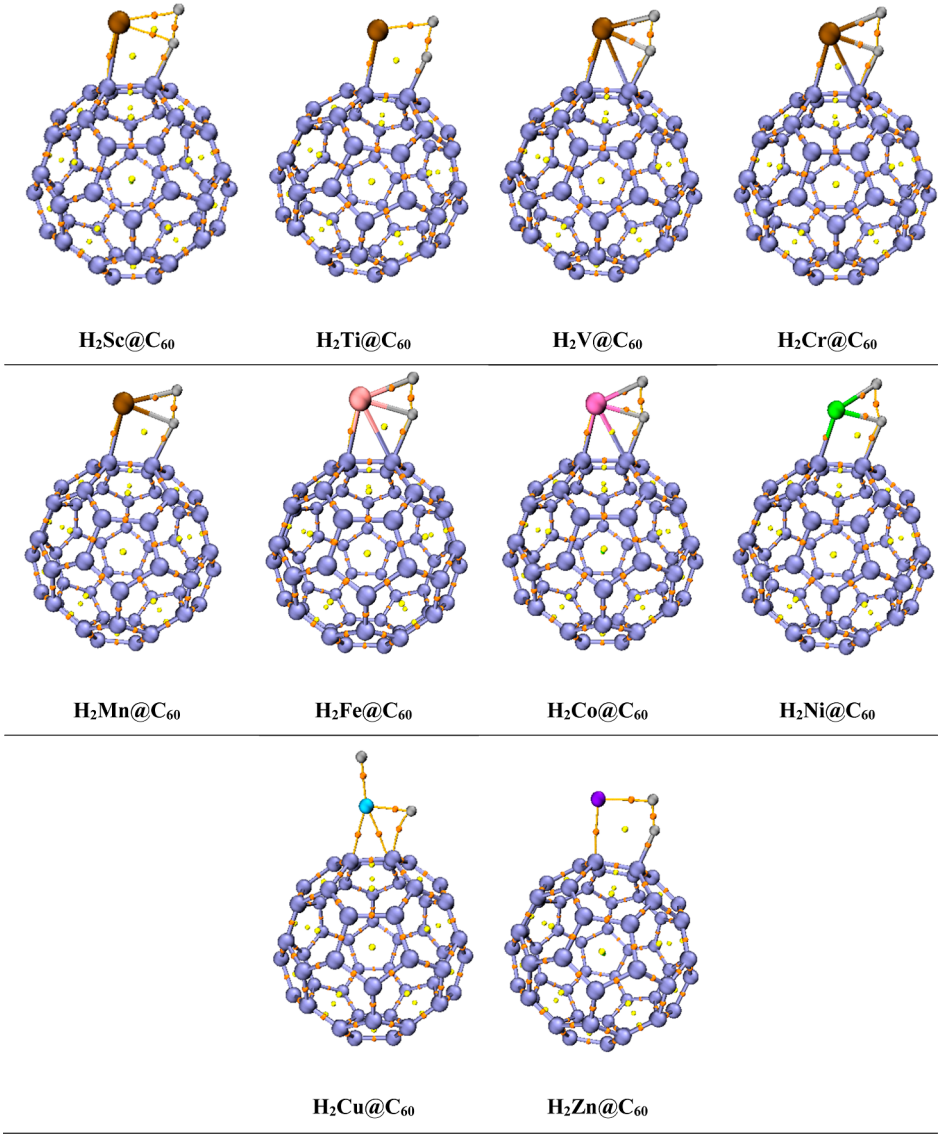


**Figure 7.** QTAIM molecular plots of the designed hydrogen-adsorbed TM@$C_{60}$ metallofullerenes.

With respect to the interaction of adsorbed hydrogen with the designed metallofullerenes, two BCPs are considered for each metallofullerene complex, as shown in Table 2. The Laplacian electron density ($\nabla^2\rho$) of computed BCPs is observed in the range of −0.118 to 0.187 for the $H_2$* + M@$C_{60}$ metallofullerenes. The value of Laplacian $\nabla^2\rho > 0$ reveals the closed shell interactions. The total energy density [$H_{(r)}$] is equivalent to the sum of $V_{(r)}$ and $G_{(r)}$, and if $H_{(r)}$ has a value less than zero ($H < 0$), it reveals covalency. For all the designed metallofullerenes, $H_{(r)}$ has a negative value and, hence, confirms the presence of shared shell or covalent interactions in the designed systems. Moreover, the ratio $-V/G$ falls in the range of 1.20 to 2.91, which further corroborates that the considered BCPs reveal shared shell or covalent interactions. These results of QTAIM analysis explicitly confirm some interatomic interactions, which are not directly possible via geometric analysis. Additionally, the QTAIM results are also consistent with the computed reactivities and adsorption energies of the designed metallofullerene complexes.

## 4. CONCLUSIONS

In the current study, we have theoretically designed and evaluated catalytic efficiency of first row TM-doped fullerenes (TM@$C_{60}$) as SACs for the HDR. Interaction energy analysis reveals that doping of TM over $C_{60}$ fullerene is an exothermic process and the highest value of interaction energy is seen for Cu@$C_{60}$ metallofullerenes (−2.13 eV). Additionally, the $H_2$ adsorption energies ($E_{ads}$) and the dissociation barriers over TM@$C_{60}$ metallofullerenes are also calculated and compared systematically for all the designed systems. The hydrogen dissociation energy profile declares that the dissociated hydrogen (2H* state) complexes are more favorable energetically due to negative energy (exothermic process). Among all the designed TM@$C_{60}$ metallofullerenes, the smallest activation energy barrier is observed for the Sc@$C_{60}$ complex (0.13 eV) followed by V@$C_{60}$ (0.19 eV). The best catalytic performance of Sc@$C_{60}$ metallofullerene is attributed to the highest NBO charge transfer from scandium (Sc) metal atoms. NBO and EDD analyses reveal the charge transfer from TM to $H_2$ molecule, resulting in filling up the antibonding orbital of $H_2$, consequently making HDR more feasible. QTAIM analysis is


https://doi.org/10.1021/acsomega.3c05477
ACS Omega 2023, 8, 36493−36505

carried out to investigate the nature of interatomic interactions between hydrogen molecules and metallofullerenes and the results show the presence of shared shell interactions. Overall, $Sc@C_{60}$ metallofullerenes can act as a remarkable noble metal free electrocatalyst for the hydrogen dissociation process, which paves a novel way for experimentalists to design highly efficient SACs for HDR.

## ■ ASSOCIATED CONTENT

### Supporting Information

The Supporting Information is available free of charge at https://pubs.acs.org/doi/10.1021/acsomega.3c05477.

Relative stabilities of $M@C_{20}$ complexes and schematic reaction pathway (PDF)

## ■ AUTHOR INFORMATION


### Corresponding Authors

**Imene Bayach** − *Department of Chemistry, College of Science, King Faisal University, Al-Ahsa 31982, Saudi Arabia;* orcid.org/0000-0003-1375-0612; Email: ibayach@kfu.edu.sa

**Nadeem S. Sheikh** − *Chemical Sciences, Faculty of Science, Universiti Brunei Darussalam, Gadong BE1410, Brunei Darussalam;* orcid.org/0000-0002-0716-7562; Email: nadeem.sheikh@ubd.edu.bn

**Khurshid Ayub** − *Department of Chemistry, COMSATS University Islamabad, Abbottabad 22060, Pakistan;* orcid.org/0000-0003-0990-1860; Email: khurshid@cuiatd.edu.pk

### Authors

**Sehrish Sarfaraz** − *Department of Chemistry, COMSATS University Islamabad, Abbottabad 22060, Pakistan*

**Muhammad Yar** − *Department of Chemistry, COMSATS University Islamabad, Abbottabad 22060, Pakistan*

**Ajaz Hussain** − *Institute of Chemical Sciences, Bahauddin Zakariya University, Multan 60800, Pakistan;* orcid.org/0000-0001-5981-9430

**Ahmed Lakhani** − *Department of Biomedical and Health Sciences, Calumet College of St. Joseph, Whiting, Indiana 46394, United States;* orcid.org/0000-0003-1086-3101

**Adnan Gulzar** − *Center of Theoretical Chemistry, Ruhr-Universitat Bochum, Bochum 44780, Germany*

**Muhammad Ans** − *Department of Chemistry, University of Agriculture Faisalabad, Faisalabad 38000, Pakistan;* orcid.org/0000-0002-5397-7435

**Umer Rashid** − *Department of Chemistry, COMSATS University Islamabad, Abbottabad 22060, Pakistan;* orcid.org/0000-0002-2419-3172

**Masroor Hussain** − *Department of Data Science, Ghulam Ishaq Khan Institute of Engineering Sciences and Technology, Topi 23460, Pakistan*

**Shabbir Muhammad** − *Department of Physics, College of Science, King Khalid University, Abha 61413, Saudi Arabia;* orcid.org/0000-0003-4908-3313

Complete contact information is available at: https://pubs.acs.org/10.1021/acsomega.3c05477


### Notes

The authors declare no competing financial interest.

## ■ ACKNOWLEDGMENTS

This work was supported by the Deanship of Scientific Research, Vice Presidency for Graduate Studies and Scientific Research, King Faisal University, Saudi Arabia [grant no. 3861]. Also, we give thanks to the Higher Education Commission of Pakistan under a HEC indigenous fellowship to Sehrish Sarfaraz (PIN) 520-141149-2PS6-178 (50093367) and COMSATS University Islamabad, Abbottabad Campus for financial support.

## ■ REFERENCES


(1) Luo, Y.-H.; Cai, Y.; Long, X.; Zhou, D.; Zhou, C.; Rittmann, B. E. Palladium (Pd0) Loading-Controlled Catalytic Activity and Selectivity for Chlorophenol Hydrodechlorination and Hydrosaturation. *Environ. Sci. Technol.* **2022**, *56*, 4447−4456.

(2) Chen, Y.; Feng, C.; Wang, W.; Liu, Z.; Li, J.; Liu, C.; Pan, Y.; Liu, Y. Electronic structure engineering of bimetallic Pd-Au alloy nanocatalysts for improving electrocatalytic hydrodechlorination performance. *Sep. Purif. Technol.* **2022**, *289*, 120731.

(3) Shi, Z.; Li, N.; Lu, H. K.; Chen, X.; Zheng, H.; Yuan, Y.; Ye, K. Y. Recent advances in the electrochemical hydrogenation of unsaturated hydrocarbons. *Curr. Opin. Electrochem.* **2021**, *28*, 100713.

(4) Sun, Z.; Wang, S.; Chen, W. Metal single-atom catalysts for selective hydrogenation of unsaturated bonds. *J. Mater. Chem. A* **2021**, *9*, 5296−5319.

(5) Borshch, V.; Pugacheva, E. V.; Zhuk, S. Y.; Smirnova, E. M.; Demikhova, N. R.; Vinokurov, V. A. Hydrogenation of CO 2 on the polymetallic catalysts prepared by self-propagating high-temperature synthesis. *Russ. Chem. Bull.* **2020**, *69*, 1697−1702.

(6) Jain, I. P. Hydrogen the fuel for 21st century. *Int. J. Hydrogen Energy* **2009**, *34*, 7368−7378.

(7) Wan, W.; Nie, X.; Janik, M. J.; Song, C.; Guo, X. Adsorption, dissociation, and spillover of hydrogen over Au/TiO2 catalysts: the effects of cluster size and metal−support interaction from DFT. *J. Phys. Chem. C* **2018**, *122*, 17895−17916.

(8) Nakamura, I.; Mantoku, H.; Furukawa, T.; Fujitani, T. Active Sites for Hydrogen Dissociation over $TiO_x$/Au(111) Surfaces. *J. Phys. Chem. C* **2011**, *115*, 16074−16080.

(9) Beheshtian, J.; Ahmadi Peyghan, A.; Bagheri, Z. Hydrogen dissociation on diene-functionalized carbon nanotubes. *J. Mol. Model.* **2013**, *19*, 255−261.

(10) Cui, Y.-H.; Tian, W. Q.; Feng, J.-K.; Chen, D.-L. Structures, stabilities, aromaticity, and electronic properties of C66 fullerene isomers, anions (C66 2-, C66 4-, C66 6-), and metallofullerenes (Sc2@C66). *J. Nanopart. Res.* **2010**, *12* (2), 429.

(11) Abe, J. O.; Popoola, A.; Ajenifuja, E.; Popoola, O. Hydrogen energy, economy and storage: Review and recommendation. *Int. J. Hydrogen Energy* **2019**, *44*, 15072−15086.

(12) Bigall, N. C.; Reitzig, M.; Naumann, W.; Simon, P.; van Pée, K. H.; Eychmüller, A. Fungal templates for noble-metal nanoparticles and their application in catalysis. *Angew. Chem.* **2008**, *120*, 7994−7997.

(13) de Beer, M.; et al. Technical and economic aspects of promotion of cobalt-based Fischer-Tropsch catalysts by noble metals-a review. *J. South. Afr. Inst. Min. Metall.* **2014**, *114*, 157−165.

(14) Zhai, P.; Xia, M.; Wu, Y.; Zhang, G.; Gao, J.; Zhang, B.; Cao, S.; Zhang, Y.; Li, Z.; Fan, Z.; et al. Engineering single-atomic ruthenium catalytic sites on defective nickel-iron layered double hydroxide for overall water splitting. *Nat. Commun.* **2021**, *12*, 4587.

(15) Lei, Y.; Wang, Y.; Liu, Y.; Song, C.; Li, Q.; Wang, D.; Li, Y. Designing atomic active centers for hydrogen evolution electrocatalysts. *Angew. Chem., Int. Ed.* **2020**, *59*, 20794−20812.

(16) Wu, J.; Xiong, L.; Zhao, B.; Liu, M.; Huang, L. Densely populated single atom catalysts. *Small Methods* **2020**, *4*, 1900540.

(17) Zhang, Z.; Masubuchi, T.; Sautet, P.; Anderson, S. L.; Alexandrova, A. N. Hydrogen Evolution on Electrode-Supported $Pt_n$ Clusters: Ensemble of Hydride States Governs the Size Dependent Reactivity. *Angew. Chem.* **2023**, *135*, No. e202218210.

(18) Xie, J.; Ng, K.; Dai, Y.; Jiang, J.; Yu, J.; Gao, A.; Wang, H.; Huang, X.; Liu, W.; Guo, S. A Novel Pd Precursor Loaded $\gamma$-$Al_2O_3$ with

Excellent Adsorbent Performance for Ultra-Deep Adsorptive Desulfurization of Benzene. *Adv. Funct. Mater.* **2023**, *33*, 2213837.
(19) Lang, R.; Du, X.; Huang, Y.; Jiang, X.; Zhang, Q.; Guo, Y.; Liu, K.; Qiao, B.; Wang, A.; Zhang, T. Single-atom catalysts based on the metal−oxide interaction. *Chem. Rev.* **2020**, *120*, 11986−12043.
(20) Piccolo, L. Restructuring effects of the chemical environment in metal nanocatalysis and single-atom catalysis. *Catal. Today* **2021**, *373*, 80−97.
(21) Su, Y.; Wu, F.; Song, Q.; Wu, M.; Mohammadniaei, M.; Zhang, T.; Liu, B.; Wu, S.; Zhang, M.; Li, A.; et al. Dual enzyme-mimic nanozyme based on single-atom construction strategy for photothermal-augmented nanocatalytic therapy in the second near-infrared biowindow. *Biomaterials* **2022**, *281*, 121325.
(22) Huo, M.; et al. Nanocatalytic tumor therapy by single-atom catalysts. *ACS Nano* **2019**, *13*, 2643−2653.
(23) Tiwari, J. N.; Singh, A. N.; Sultan, S.; Kim, K. S. Recent Advancement of p- and d-Block Elements, Single Atoms, and Graphene-Based Photoelectrochemical Electrodes for Water Splitting. *Adv. Energy Mater.* **2020**, *10*, 2000280.
(24) Sultan, S.; Tiwari, J. N.; Singh, A. N.; Zhumagali, S.; Ha, M.; Myung, C. W.; Thangavel, P.; Kim, K. S. Single atoms and clusters based nanomaterials for hydrogen evolution, oxygen evolution reactions, and full water splitting. *Adv. Energy Mater.* **2019**, *9*, 1900624.
(25) Xi, J.; Jung, H. S.; Xu, Y.; Xiao, F.; Bae, J. W.; Wang, S. Synthesis strategies, catalytic applications, and performance regulation of single-atom catalysts. *Adv. Funct. Mater.* **2021**, *31*, 2008318.
(26) Deng, C.; He, R.; Shen, W.; Li, M.; Zhang, T. A single-atom catalyst of cobalt supported on a defective two-dimensional boron nitride material as a promising electrocatalyst for the oxygen reduction reaction: a DFT study. *Phys. Chem. Chem. Phys.* **2019**, *21*, 6900−6907.
(27) Liu, J.; Xiao, J.; Luo, B.; Tian, E.; Waterhouse, G. I. Central metal and ligand effects on oxygen electrocatalysis over 3d transition metal single-atom catalysts: A theoretical investigation. *Chem. Eng. J.* **2022**, *427*, 132038.
(28) Ha, M.; Kim, D. Y.; Umer, M.; Gladkikh, V.; Myung, C. W.; Kim, K. S. Tuning metal single atoms embedded in N x C y moieties toward high-performance electrocatalysis. *Energy Environ. Sci.* **2021**, *14*, 3455−3468.
(29) Meng, X.; Liu, X.; Fan, X.; Chen, X.; Chen, S.; Meng, Y.; Wang, M.; Zhou, J.; Hong, S.; Zheng, L.; et al. Single-Atom Catalyst Aggregates: Size-Matching is Critical to Electrocatalytic Performance in Sulfur Cathodes. *Adv. Sci.* **2022**, *9*, 2103773.
(30) Shang, Y.; Duan, X.; Wang, S.; Yue, Q.; Gao, B.; Xu, X. Carbon-based single atom catalyst: Synthesis, characterization, DFT calculations. *Chin. Chem. Lett.* **2022**, *33*, 663−673.
(31) Feng, Y.; Wan, Q.; Xiong, H.; Zhou, S.; Chen, X.; Pereira Hernandez, X. I.; Wang, Y.; Lin, S.; Datye, A. K.; Guo, H. Correlating DFT Calculations with CO Oxidation Reactivity on Ga-Doped Pt/CeO2 Single-Atom Catalysts. *J. Phys. Chem. C* **2018**, *122*, 22460−22468.
(32) Gao, Y.; Cai, Z.; Wu, X.; Lv, Z.; Wu, P.; Cai, C. Graphdiyne-Supported Single-Atom-Sized Fe Catalysts for the Oxygen Reduction Reaction: DFT Predictions and Experimental Validations. *ACS Catal.* **2018**, *8*, 10364−10374.
(33) Yang, W.; Gao, Z.; Liu, X.; Ma, C.; Ding, X.; Yan, W. Directly catalytic reduction of NO without NH3 by single atom iron catalyst: A DFT calculation. *Fuel* **2019**, *243*, 262−270.
(34) Pan, Y.; Liu, X.; Zhang, W.; Liu, Z.; Zeng, G.; Shao, B.; Liang, Q.; He, Q.; Yuan, X.; Huang, D.; et al. Advances in photocatalysis based on fullerene C60 and its derivatives: Properties, mechanism, synthesis, and applications. *Appl. Catal., B* **2020**, *265*, 118579.
(35) Bibikov, A.; Nikolaev, A. V.; Bodrenko, I. V.; Borisyuk, P. V.; Tkalya, E. V. Multiple locations of boron atoms in the exohedral and endohedral C 60 fullerene. *Phys. Rev. A* **2022**, *105*, 022813.
(36) Vizuete, M.; Barrejón, M.; Gómez-Escalonilla, M. J.; Langa, F. Endohedral and exohedral hybrids involving fullerenes and carbon nanotubes. *Nanoscale* **2012**, *4*, 4370−4381.
(37) Zhan, S.-Z.; Zhang, G. H.; Li, J. H.; Liu, J. L.; Zhu, S. H.; Lu, W.; Zheng, J.; Ng, S. W.; Li, D. Exohedral cuprofullerene: sequentially expanding metal olefin up to a C60@ Cu24 rhombicuboctahedron. *J. Am. Chem. Soc.* **2020**, *142*, 5943−5947.
(38) He, M.; Han, S.; Xu, Z.; Liu, G.; Qiao, G. Electrocatalytic properties of scandium metallofullerenes for the hydrogen evolution reaction. *Int. J. Hydrogen Energy* **2022**, *47*, 11904−11915.
(39) Wen, S.-H.; Deng, W.-Q.; Han, K.-L. Endohedral BN metallofullerene M@ B36N36 complex as promising hydrogen storage materials. *J. Phys. Chem. C* **2008**, *112*, 12195−12200.
(40) He, T.; Gao, G.; Kou, L.; Will, G.; Du, A. Endohedral metallofullerenes (M@ C60) as efficient catalysts for highly active hydrogen evolution reaction. *J. Catal.* **2017**, *354*, 231−235.
(41) Robledo, M.; Díaz-Tendero, S.; Martín, F.; Alcamí, M. Theoretical study of the interaction between molecular hydrogen and [MC60]+ complexes. *RSC Adv.* **2016**, *6*, 27447−27451.
(42) Hamamoto, N.; Jitsukawa, J.; Satoko, C. Electronic and geometric properties of alkali-C 60 molecules. *Eur. Phys. J. D* **2002**, *19*, 211−221.
(43) Ma, L.-J.; Hao, W.; Wang, j.; Jia, J.; Wu, H. S. Sc/Ti-decorated and B-substituted defective C60 as efficient materials for hydrogen storage. *Int. J. Hydrogen Energy* **2021**, *46*, 14508−14519.
(44) Naghshineh, N.; Hashemianzadeh, M. First-principles study of hydrogen storage on Si atoms decorated C60. *Int. J. Hydrogen Energy* **2009**, *34*, 2319−2324.
(45) Frisch, M. J.; et al. *Gaussian 09*, Revision B. 01; Gaussian, Inc.: Wallingford, CT, 2009.
(46) Tahir, H.; Kosar, N.; Ayub, K.; Mahmood, T. Outstanding NLO response of thermodynamically stable single and multiple alkaline earth metals doped C20 fullerene. *J. Mol. Liq.* **2020**, *305*, 112875.
(47) Sarfaraz, S.; Yar, M.; Hussain, R.; Ayub, K. Adsorption and dissociation of H2 molecule over first-row transition metal doped C24 nanocage as remarkable SACs: A comparative study. *Int. J. Hydrogen Energy* **2023**, *48*, 20633−20645.
(48) Bibi, S.; Sarfaraz, S.; Yar, M.; Zaman, M. I.; Niaz, A.; Khan, A.; Hashmi, M. A.; Ayub, K. Structure and electronic characterization of pristine and functionalized single wall carbon nanotube interacting with sulfide ion: A density functional theory approach. *J. Mol. Liq.* **2022**, *366*, 120144.
(49) Allangawi, A.; Mahmood, T.; Ayub, K.; Gilani, M. A. Anchoring the late first row transition metals with B12P12 nanocage to act as single atom catalysts toward oxygen evolution reaction (OER). *Mater. Sci. Semicond. Process.* **2023**, *153*, 107164.
(50) Mukhtar, A.; Sarfaraz, S.; Ayub, K. Organic transformations in the confined space of porous organic cage CC2; catalysis or inhibition. *RSC Adv.* **2022**, *12*, 24397−24411.
(51) Shah, A. B.; Sarfaraz, S.; Yar, M.; Sheikh, N. S.; Hammud, H. H.; Ayub, K. Remarkable Single Atom Catalyst of Transition Metal (Fe, Co & Ni) Doped on C2N Surface for Hydrogen Dissociation Reaction. *Nanomaterials* **2022**, *13*, 29.
(52) Dennington, R.; Keith, T.; Millam, J. *GaussView*, version 8; Semichem Inc.: Shawnee Mission KS, 2009; Vol. *5*.
(53) Sarfaraz, S.; Yar, M.; Ali Khan, A.; Ahmad, R.; Ayub, K. DFT investigation of adsorption of nitro-explosives over C2N surface: Highly selective towards trinitro benzene. *J. Mol. Liq.* **2022**, *352*, 118652.
(54) Al-Faiyz, Y. S.; Sarfaraz, S.; Yar, M.; Munsif, S.; Khan, A. A.; Amin, B.; Sheikh, N. S.; Ayub, K. Efficient Detection of Nerve Agents through Carbon Nitride Quantum Dots: A DFT Approach. *Nanomaterials* **2023**, *13*, 251.
(55) Sarfaraz, S.; et al. Transition Metal-Doped C20 Fullerene-Based Single-Atom Catalysts with High Catalytic Activity for Hydrogen Dissociation Reaction. *ACS Omega* **2023**, *8*, 14077−14088.
(56) Lu, T.; Chen, F. Multiwfn: A multifunctional wavefunction analyzer. *J. Comput. Chem.* **2012**, *33*, 580−592.
(57) Sabet, M.; Tanreh, S.; Khosravi, A.; Astaraki, M.; Rezvani, M.; Darvish Ganji, M. Theoretical assessment of the solvent effect on the functionalization of Au32 and C60 nanocages with fluorouracil drug. *Diamond Relat. Mater.* **2022**, *126*, 109142.
(58) Omidvar, A.; Mohajeri, A. Decoration of doped C60 fullerene with alkali metals: Prototype nanomaterial with enhanced binding


https://doi.org/10.1021/acsomega.3c05477
*ACS Omega* 2023, 8, 36493−36505

energy toward hydrogen. *Int. J. Hydrogen Energy* **2017**, *42*, 12327−12338.
(59) Sarfaraz, S.; Yar, M.; Ayub, K. Covalent triazine framework (CTF-0) surface as a smart sensing material for the detection of CWAs and industrial pollutants. *Mater. Sci. Semicond. Process.* **2022**, *139*, 106334.
(60) Youn, I. S.; Kim, D. Y.; Singh, N. J.; Park, S. W.; Youn, J.; Kim, K. S. Intercalation of Transition Metals into Stacked Benzene Rings: A Model Study of the Intercalation of Transition Metals into Bilayered Graphene. *J. Chem. Theory Comput.* **2012**, *8*, 99−105.
(61) Wang, X.; Liew, K. M. Density functional study of interaction of lithium with pristine and Stone-Wales-defective single-walled silicon carbide nanotubes. *J. Phys. Chem. C* **2012**, *116*, 26888−26897.
(62) Bezi Javan, M.; Houshang Shirdel-Havar, A.; Soltani, A.; Pourarian, F. Adsorption and dissociation of H2 on Pd doped graphene-like SiC sheet. *Int. J. Hydrogen Energy* **2016**, *41*, 22886−22898.
(63) Wu, H.; Fan, X.; Kuo, J.-L. Metal free hydrogenation reaction on carbon doped boron nitride fullerene: A DFT study on the kinetic issue. *Int. J. Hydrogen Energy* **2012**, *37*, 14336−14342.
(64) Mahamiya, V.; Shukla, A.; Chakraborty, B. Scandium decorated C24 fullerene as high capacity reversible hydrogen storage material: insights from density functional theory simulations. *Appl. Surf. Sci.* **2022**, *573*, 151389.
(65) Corma, A.; Boronat, M.; González, S.; Illas, F. On the activation of molecular hydrogen by gold: a theoretical approximation to the nature of potential active sites. *Chem. Commun.* **2007**, *32*, 3371−3373.
(66) Sun, K.; Kohyama, M.; Tanaka, S.; Takeda, S. A study on the mechanism for H2 dissociation on Au/$TiO_2$ catalysts. *J. Phys. Chem. C* **2014**, *118*, 1611−1617.


https://doi.org/10.1021/acsomega.3c05477
*ACS Omega* 2023, 8, 36493−36505